Distributed energy balance modeling of South Cascade Glacier, Washington and assessment of model uncertainty

Faron S. Anslow,[1,2] Steven Hostetler,[3] William R. Bidlake,[4] and Peter U. Clark[1]

[1] We have developed a physically based, distributed surface energy balance model to simulate glacier mass balance under meteorological and climatological forcing. Here we apply the model to estimate summer ablation on South Cascade Glacier, Washington, for the 2004 and 2005 mass balance seasons. To arrive at optimal mass balance simulations, we investigate and quantify model uncertainty associated with selecting from a range of physical parameter values that are not commonly measured in glaciological mass balance field studies. We optimize the performance of the model by varying values for atmospheric transmissivity, the albedo of surrounding topography, precipitation-elevation lapse rate, surface roughness for turbulent exchange of momentum, and snow albedo aging coefficient. Of these the snow aging parameter and precipitation lapse rates have the greatest influence on the modeled ablation. We examined model sensitivity to varying parameters by performing an additional 10^3 realizations with parameters randomly chosen over a $\pm 5\%$ range centered about the optimum values. The best fit suite of model parameters yielded a net balance of -1.69 ± 0.38 m water equivalent (WE) for the 2004 water year and -2.10 ± 0.30 m WE up to 11 September 2005. The 2004 result is within 3% of the measured value. These simulations account for 91% and 93% of the variance in measured ablation for the respective years.

1. Introduction

[2] The Earth's cryosphere is changing rapidly, as characterized by worldwide glacier and sea ice loss that has been occurring over the past century and accelerated during the last decade [*Arendt et al.*, 2002; *Dyurgerov*, 2003; *Kaser et al.*, 2006]. Numerical glacier models quantify the sensitivity of alpine glaciers to climate, and provide tools for evaluating the closely related response of ecosystems and water resources in glacierized regions of the world. Ideally, glacier models should be suitable for several applications: (1) to locations where meteorological forcing data are locally measured such as *Arnold et al.* [1996]; (2) to remote glaciers for which some or all input data must be derived from distant stations as by *Gerbaux et al.* [2005]; (3) to glaciers whose input data is provided by atmospheric models [*Bougamont et al.*, 2007]; and (4) finally to former glaciers for paleoclimate application [*Plummer and Phillips*, 2003; *Laabs et al.*, 2006]. In this paper we develop a model

and analyze its sensitivity to measurements and parameterizations with the above applications in mind. Our aim is to quantify the uncertainty that arises in making even well-founded assumptions about the physical parameters that govern the model results as well as the model uncertainty that arises because of uncertainty in the input meteorological variables.

[3] Physically based models of the glacier surface energy balance (SEBM) account for the heat inputs and losses to a glacier surface and are detailed enough to capture most of the physical processes that govern surface melt. Surface energy balance calculations have been made over glaciers at the point scale [*Munro*, 1990; *Marks and Dozier*, 1992; *Greuell and Konzelmann*, 1994; *Brock and Arnold*, 2000], along centerlines [*Oerlemans and Hoogendoorn*, 1989; *Oerlemans*, 1992] and in spatially distributed form [*Escher-Vetter*, 1985; *Arnold et al.*, 1996; *Klok and Oerlemans*, 2002; *Hock and Holmgren*, 2005]. These models differ from the commonly used empirical ablation models such as the Positive Degree Day (PDD) model of *Braithwaite* [1981], the temperature/solar radiation index model developed by *Hock* [1999] and the enhanced temperature index model developed by *Pellicciotti et al.* [2005], which use empirical relationships between several (i.e., temperature, solar, precipitation) meteorological variables and surface melt. Because SEBMs can be formulated to be driven by a relatively small set of meteorological data, they are readily applied anywhere forcing data are measured or obtainable. The physical complexity of SEBMs introduces a

[1]Department of Geosciences, Oregon State University, Corvallis, Oregon, USA.
[2]Now at Department of Earth and Ocean Sciences, University of British Columbia, Vancouver, British Columbia, Canada.
[3]United States Geological Survey, Department of Geosciences, Oregon State University, Corvallis, Oregon, USA.
[4]United States, Geological Survey, Washington Water Science Center, Tacoma, Washington, USA.
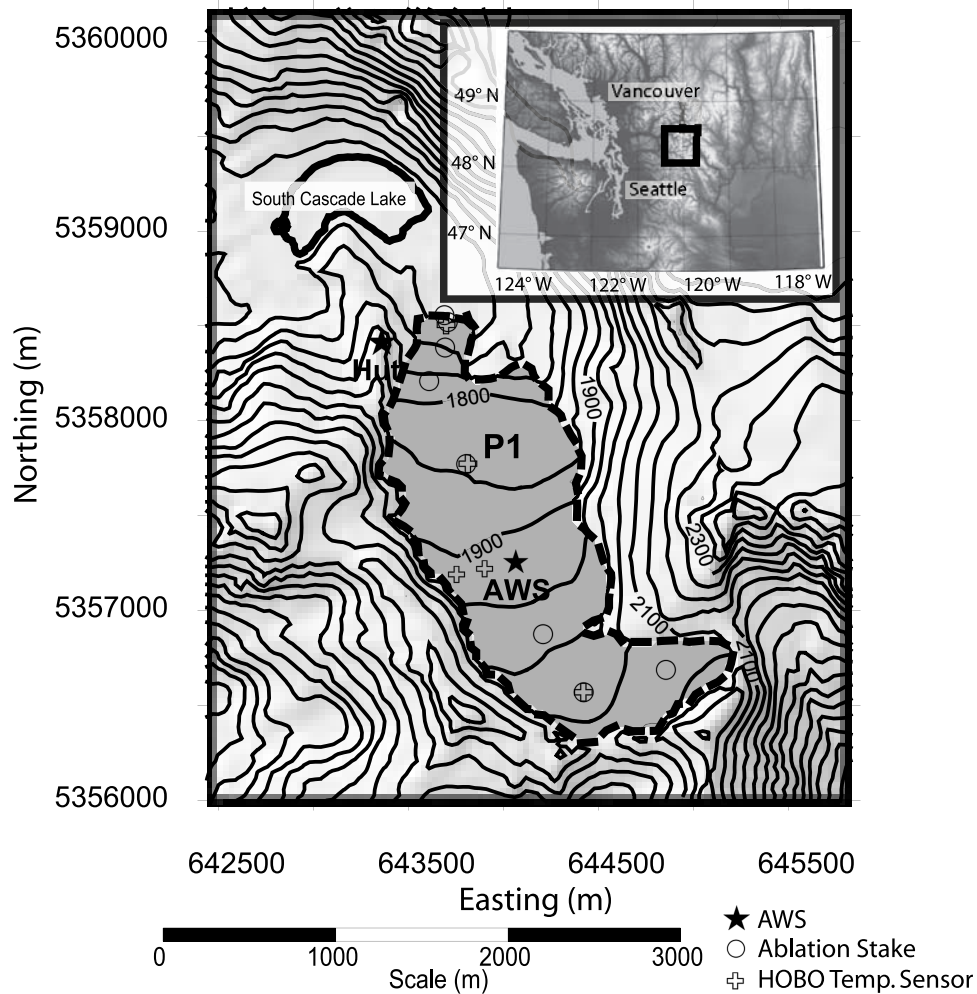
Figure 1. Locations of AWS, ablation measurement sites, and HOBO temperature loggers are indicated. Inset shows South Cascade Glacier study area relative to state of Washington and surrounding cities.

larger parameter space than do the empirical models mentioned above, so justifying the use of SEBMs requires quantification of the influence of those parameters on model performance both parameter by parameter and as a whole. In most studies using SEBMs, the authors quantify the sensitivity to individual parameters, to secular changes in input variables, or to changes in surface geometry [*Klok and Oerlemans*, 2002; *Klok and Oerlemans*, 2004; *Gerbaux et al.*, 2005; *Hock and Holmgren*, 2005; *Klok et al.*, 2005; *Arnold et al.*, 2006]. We aim to assess the effects on model results of simultaneously varying multiple parameters governing the model.

[4] In this paper we introduce a SEBM developed using data from South Cascade Glacier (SCG), Washington, United States, a glacier that has been monitored by the U.S. Geological Survey for nearly 50 years. We apply the model to explore the sensitivity of summer ablation to variations in six of the physical parameters that primarily govern the physics of the model: precipitation lapse rate, surface roughness of snow, surface roughness of ice, the broadband albedo of surrounding terrain, the atmosphere's transmissivity to solar radiation, and the aging parameter for snow albedo. The model is fitted to measured ablation data

from the ongoing SCG mass balance program and then parameters are perturbed to judge the error in estimating mass balance that occurs with uncertainty in a given parameter. We also estimate uncertainties in model results due to errors in the input meteorological data. These analyses together quantify much of the uncertainty inherent in applying a SEBM.

2. Methods

2.1. Field Site

[5] SCG is a small (1.8 km^2) north-facing alpine valley glacier located in the North Cascades Mountains (Lat. 48° 20′N, Lon. 121°3′W). The gently sloping glacier surface has an altitude range of ~1600–~2100 m over a 3 km centerline length (Figure 1). Rugged topography surrounds the glacier, with relief exceeding 1500 m and peaks reaching 2400 m elevation. SCG lies on the west side of the divide that separates eastward drainage into the Columbia River from westward drainage into the Skagit River via the South Fork of the Cascade River. The maritime climate of the glacier basin is characterized by extremes of winter accumulation approaching 5 m water equivalent (WE) on the upper

Table 1. Instrumentation Used in This Study

Variable	Instrument	Precision
Temperature	Humidity and Temperature Probe 50	±0.5°C
Relative Humidity	Humidity and Temperature Probe 50	±4%
Wind	Met One 014A	±1.5%
Broadband Solar Radiation	Eppley Precision Spectral Pyranometer	±2%
Downwelling Longwave	Eppley Precision Infrared Radiometer	±2%
Precipitation	Texas Electronics Tipping Bucket	±1%
Backup Solar Radiation	Li-Cor LI-200	≤5%
Temperature	Onset HOBO Pro	±0.2°C
Surface Height Lowering	Judd Communications Ultrasonic Depth Sensor	±0.4%

elevations and by summer net losses of >9 m WE at the terminus during high-ablation years.

[6] Continuous monitoring and research of SCG began during the first International Geophysical Year in 1957 by the United States Geological Survey [*Meier*, 1958] which has maintained records of and continues to measure mass balance and outlet stream discharge since inception of the program. Meteorological and hydrological measurements have been made sporadically over the research history of SCG. Annual data summaries of mass balance, hydrological, and meteorological measurements are published in the form of USGS Scientific Investigations Reports (e.g., *Bidlake et al.* [2007], available from the USGS Washington Water Science Center, http://wa.water.usgs.gov/). The digital elevation model used in this research is derived from stereo photography referenced to the 2002 glacier surface. These data were supplied by the USGS Washington Water Science Center.

2.2. Meteorological Measurements

[7] An automatic weather station (AWS) has been operated year-round at the USGS research hut (located ~500 m west and ~100 m above the glacier, Figure 1) throughout the duration of the mass balance measurement program with temperature, humidity, and precipitation data consistently measured. For this research the suite of AWS measurements was expanded to wind speed, air temperature, relative humidity, incoming global shortwave radiation, incoming atmospheric longwave radiation, and liquid precipitation. An additional Li-Cor shortwave radiometer has been deployed continuously for the past several years and was used as a backup to the Eppley pyranometer. The instrument types and their rated measurement errors are outlined in Table 1. The instruments are mounted ~5 m above an uneven ridge top. Precipitation is also measured at the Salix Creek stream gauging site at an elevation of 1580 m for use during periods when snowfall affects the hut precipitation gauge. Measurements were made at minute resolution and averaged to hourly records.

[8] During the periods July–September 2004 and May–September 2005, an additional AWS was deployed on the glacier surface at an elevation of 1950 m to provide over-glacier wind speed, temperature and humidity data for turbulent heat flux calculations. The AWS recorded wind speed, air temperature, and humidity at 1.9 m above the glacier surface. This AWS was free to settle with the ablating surface and was within ±5° of vertical when visited at roughly monthly intervals. Surface air temperatures over the glacier were measured using HOBO proinstruments at three additional points roughly along the centerline of the

glacier: near the toe at 1670 m during 2004 (1636 m during 2005), midway up-glacier at 1844 m (1842 m during 2005) and in the accumulation area at 2032 m (2029 m during 2005). These instruments were also free to lower with the ablating surface. The effects of accumulation events on these measurements are thought to be small.

[9] The modeling period covers the 2004 ablation season beginning on 1 April, although the more accurate shortwave and longwave instruments were not installed until 21 July 2004. The record of shortwave and longwave measurements was extended back to 1 April using empirical relationships that were developed with measured data from the remainder of the 2004 ablation season. The shortwave record was extended with the Li-Cor instrument using a calibration between the two instruments. For longwave other authors have made estimates using air temperature, water-vapor mixing ratio, and measurements of cloud cover [*Brutsaert*, 1975; *Konzelmann et al.*, 1994]. These approaches are useful where supporting observations are available. Cloud cover measurements are not locally available so indirect derivation from measured solar radiation is possible only during daylight.

[10] Lacking an independent, continuous estimate of cloud cover, we derive an empirical relationship between effective emissivity of the atmosphere and relative humidity. Effective emissivity is computed from the ratio of measured to calculated potential (using measured air temperature and the Stephan-Boltzman law) incoming longwave radiation. At SCG, effective emissivity is related to relative humidity as a step function and was modeled as a third-order polynomial (coefficients listed in Table 2) function of relative humidity (Figure 2). Effective atmospheric emissivity is ~0.73 for relative humidity measurements up to ~65% and then increases abruptly to values near 1.0 at humidities >80%, indicative of the transition between cloudy and cloud-free conditions. Over the calibration period, the measured and simulated longwave radiation are correlated with $r = 0.73$. The mean difference between the two records is 0.0 W m^{-2} and the standard deviation of the difference is 19.2 W m^{-2}. This relationship is also used in modeling to assist in distributing longwave radiation across the glacier.

2.3. Mass Balance Measurements

[11] Field measurements of mass balance and monthly ablation were used as simulation targets for the SEBM. Winter balance was measured by the USGS in late April 2004 and mid-May 2005. A reference accumulation was measured near the terminus and at the principal reference

Table 2. Model Parameters

Symbol	Description	Value and Units
a_{decay}	Albedo Decay Rate With Temperature	Var ln $(°C)^{-1a}$
a_1	Background Albedo Parameters	0.12
a_2	Background Albedo Parameters	40 m
a_3	Background Albedo Parameters	0.3
C_p	Specific Heat Capacity of Dry Air	1004 J K^{-1} kg^{-1}
C_i	Specific Heat Capacity of Ice	2097 J K^{-1} kg^{-1}
d_0	Scale Length for Snow Transmissivity	2.5 cm WE
g	Gravitational Acceleration	9.807 m s^{-2}
k	Vonkarman Constant	0.4
P_0	Sea Level Pressure	101,325 Pa
R	Dry Air Gas Constant	287.05 J K^{-1} kg^{-1}
$R*$	Water Vapor Gas Constant	461.5 J K^{-1} kg^{-1}
S_0	Solar Constant	1365 W m^{-2}
z_I	Instrument Height	1.85 m
z_0	Surface Roughness Length	Var m^a
$\alpha_{terrain}$	Albedo of Surrounding Terrain	Var[a]
β_0	Humidity-Emissivity Relationship Coefficients	0.66
β_1	Humidity-Emissivity Relationship Coefficients	$2.2 \times 10^{-3}\%^{-1}$
β_2	Humidity-Emissivity Relationship Coefficients	$-2.5 \times 10^{-5}\%^{-2}$
β_3	Humidity-Emissivity Relationship Coefficients	$4.2 \times 10^{-7}\%^{-3}$
Γ_p	Precipitation Lapse Rate	Var km^{-1a}
ε_i	Ice Emissivity	0.98
ε_r	Rock Emissivity	0.95
ρ	Density of Ice	900 kg m^3
σ	Stefan-Boltzmann Constant	5.67×10^{-8} W m^{-2} K^{-4}
ψ	Atmospheric Transmissivity	Var[a]

[a]Denotes that parameter varied in this study.

point (termed P-1) located at midglacier in 2004. In 2005, reference accumulation was measured at the terminus, P-1 and at ~2050 m. Snow depth was probed at roughly 100 m horizontal intervals along the glacier centerline in both years and mean snow density was scaled between reference sites. In 2005, the snow depth assessment was after net ablation had begun for the season, so snow depths were assigned

from a more limited depth probing conducted in mid-April of that year. The spatial distribution of measurements are restricted to the glacier centerline because of crevasses and avalanche threat. The reader is referred to *Bidlake et al.* [2007] for specific descriptions of the year 2004 and 2005 mass balance methodology.
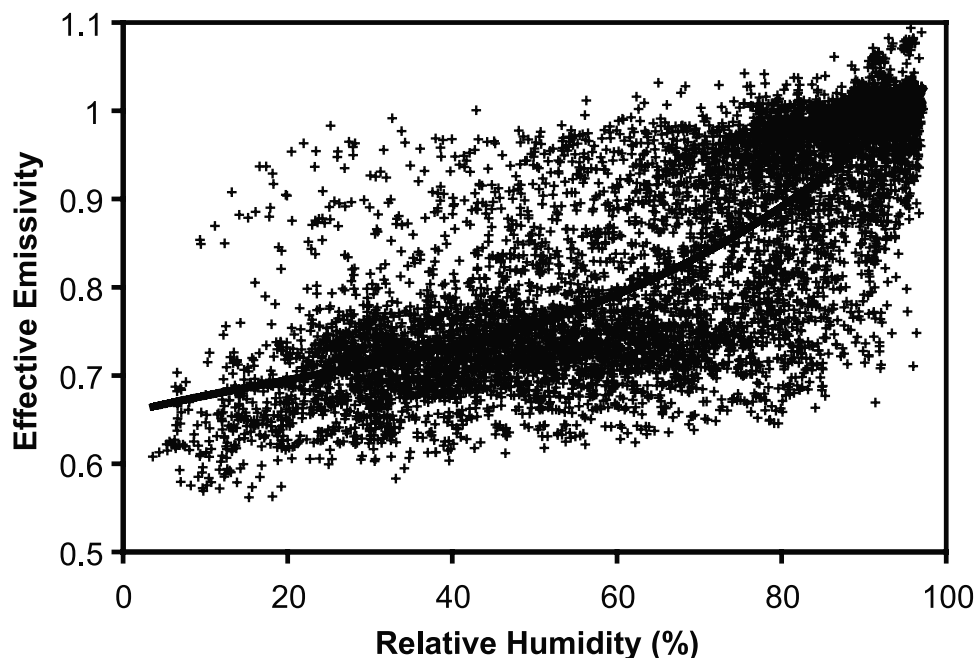
Figure 2. Relationship between effective atmospheric emissivity and relative humidity at the Hut AWS for 2004. The solid black line represents the third-order polynomial covering the transition from cloud-free to thick cloud conditions where emissivity reaches 1.

[12] Water equivalent ablation is computed as a product of the observed surface height change and material density. The ablation measurement network consisted of 9 stakes in 2004 and 6 stakes in 2005. The lower number of stakes in 2005 was due to attrition due to melt out or inaccessibility in let season. The ablation stakes are used as references for surface height change (Figure 1). Measurements were made at roughly monthly intervals Beginning 24 April 2004 through 27 October 2004, and beginning 20 April 2005 through 22 October 2005. For 2004 the density for ablated snow was estimated to be 440 kg m^3 in early season increasing to 510 kg m^3 for late season ablation. For 2005 the densities of 450 kg m^3 in early season and increasing to 530 kg m^3 in late season were applied. The density of ice for both years was taken as 900 kg m^3 [*Bidlake et al.*, 2007]. Our approach to measuring ablation does not explicitly account for errors in surface height change measurements due to compaction of the snowpack. Compaction probably had a small impact on these measurements on the basis of the small change in density of the deepest layers of the snowpack from early to late season measurements. The previous winter's accumulation was lost at ablation measurement sites by early August in 2004 and by early September in 2005. We estimate an uncertainty of ±0.1 m WE for ablation measurements and in the water year net balance estimate as estimated by *Krimmel* [2002]. This error estimate is in keeping with previously made error assessments such as *Braithwaite et al.* [1998] and *Østrem and Haakensen* [1999], however, *Bidlake et al.* [2007] emphasizes that the uncertainty in mass balance measurements on SCG is difficult to quantify on the basis of the limited spatial coverage of measurements which do not include wind deposition nor wind scour effects that could be present at the glacier margin.

[13] Additional measurements of surface lowering were made in summer, 2005, using two sonic snow depth sensors (SDS; see Table 1 for instrument information). One SDS was placed at the glacier AWS and the other was placed at the 1650 m level (Figure 1), just above the glacier toe at the location of the lowermost HOBO temperature sensor. The sensor at the AWS was operational beginning on 11 May and the lower sensor was installed on 13 July. Both sensors recorded continuously and were removed on 9 September. It is likely that the expansion/contraction of the metal mounting apparatus is responsible for some of the diurnal fluctuation observed in the data [*Willis et al.*, 2002], but the longer-term trend of the measurements is likely accurate to instrumental precision (±0.4%). This is supported by nearby stake-based measurements. Surface-height measurements recorded by the SDS were converted to water equivalent using the densities outlined above.

2.4. Distributed Energy Balance Modeling

[14] The distributed SEBM is governed by the energy balance equation

$$\rho C_i \delta h \frac{dT_s}{dt} = S_{net} + L_{net} + H_s + H_l + K + C + M - E, \quad (1)$$

where S_{net} is solar radiation balance, L_{net} is longwave radiation balance, H_s is sensible heat flux, H_l is latent heat flux, K is the geothermal heat flux, C is heat conduction into the snowpack, M is heat contributed by rain falling at temperature >0°C, E is energy for melting or refreezing, ρ is ice density in kg m^{-3}, C_i is specific heat capacity of ice in J K^{-1} kg^{-1}, δh is a small element of thickness in m, T_s is surface temperature in °C, and t is time in s. All fluxes have units W m^{-2} and are defined positive toward the surface. The glacier is assumed to be at steady state and isothermal, which eliminates the energy storage term on the left hand side of equation (1) allowing total melt (E) to be set equal to the energy input terms. The isothermal assumption simplifies equation (1) further by eliminating the geothermal heat flux term (K) and simplifying the conduction term (C) when air temperature is above the melting point. An exception to isothermal conditions is allowed at the skin of the glacier, which tracks the measured air temperature when subfreezing conditions are present. The ramifications of assuming isothermal conditions with varying surface temperature will be discussed further. In addition, the energetic contribution of precipitation (M) is assumed to be small relative to the other energy terms so is neglected.

2.4.1. Solar Radiation

[15] The solar radiation (wavelengths of 0.285−2.8 μm) impinging on a grid cell depends on direct and diffuse components that are influenced by cloud cover, surface orientation, and topographic shading. Solar position is calculated using the algorithm of *Walraven* [1978]. Terrain slope, aspect, and topographic shading are derived from the digital elevation model of the glacier and surrounding topography using a terrain computation technique based on work by *Dozier and Frew* [1990] and *Arnold et al.* [1996].

[16] Diffuse solar radiation is derived from atmospheric scattering due to aerosols and clouds, multiple reflection between terrain and clouds, and radiation reflected from surrounding topography. Partitioning measured radiation into direct and diffuse components is done through the ratio of potential to measured radiation values following *Hock and Holmgren* [2005]

$$G_{pot} = S_0 \cdot (1 - \iota)^2 \psi^{\frac{P}{P_s \cdot \sin(\theta_0)}}. \quad (2)$$

Potential radiation (G_{pot}) is calculated using the relationship expressed by *Iqbal* [1983] which is given in equation (2). Potential radiation is a function of the solar constant (S_o) adjusted for the earth-sun distance, ι, atmospheric transmissivity, ψ, adjusted for pressure P, and solar elevation angle θ_o (physical parameters are described in Table 2). Calculated potential radiation is compared to measured solar radiation, G_m, to calculate the diffuse fraction, f

$$f = \begin{cases} 0.2 & \frac{G_m}{G_{pot}} \geq 0.8 \\ -2 \cdot \frac{G_m}{G_{pot}} + 1.8 & 0.4 \leq \frac{G_m}{G_{pot}} < 0.8 \\ 1 & \frac{G_m}{G_{pot}} < 0.4 \end{cases}. \quad (3)$$

Under completely overcast skies, some fraction of the potential atmospheric radiation will be transmitted as 100% diffuse. Under clear-sky conditions the measured global radiation will have a small component of diffuse radiation

due to atmospheric scattering. In this work, the end-member for completely cloudy conditions is a $G_m:G_{\text{pot}}$ of 0.4. Ratios ≥ 0.8 are assumed to represent completely clear skies with diffuse component equal to 20% of the measured incoming radiation. A linear relationship is used between these two end-members (equation (3)). This approach follows a relationship derived by *Collares-Pereira and Rabl* [1979] and applied to alpine glaciers by *Hock and Holmgren* [2005] who developed a similar relationship for measurements made near Storglaciären, Sweden. The diffuse component and direct radiation component are calculated utilizing f from equation (3)

$$G_{\text{dif}} = \frac{G_m}{\sin(\theta_0)} f \qquad (4)$$

$$G_{\text{dir}} = \frac{G_m}{\sin(\theta_0)}(1 - f). \qquad (5)$$

The $\sin(\theta_o)$ terms adjust measured radiation for the elevation angle of the sun at the time of measurement and the results G_{diff} and G_{dir} represent the diffuse and direct radiation components.

[17] Diffuse radiation received from surrounding slopes is incorporated by considering the hemispheric fraction of terrain viewable at a given grid cell and, conversely, the fraction of viewable sky which is calculated using the algorithm of *Dozier and Frew* [1990]

$$G = [G_{\text{dif}} + G_{\text{dir}} \cdot \cos(\Theta)](\Phi) + G_{\text{dir}}\alpha_{\text{terrain}}(1 - \Phi). \qquad (6)$$

The radiative contribution from surrounding slopes is the product of direct radiation, the albedo of the surrounding terrain and the fraction of sky obscured by terrain, which ranges from 5% to 65%. In equation (6) Φ is the skyview fraction, Θ is the angle between the solar beam and the vector normal to the grid cell in question. This angle is calculated by calculating the dot product between the unit vector representing the direction of the solar beam with the unit vector normal to the grid cell in question

$$\cos(\Theta) = \cos(\theta_0)\sin(\theta) + \sin(\theta_0)\cos(\theta)\cos(\phi_0 - \phi). \qquad (7)$$

That dot product is expressed in equation (7) in which θ represents the solar elevation angle, ϕ is the solar azimuth angle, θ_0 is the slope angle, and ϕ_0 is aspect. Absorbed shortwave radiation is computed from G by adjusting for surface albedo

$$S_{\text{net}} = (1 - \alpha)G. \qquad (8)$$

In equation (8), S_{net} is net solar radiation, and α is albedo.

2.4.2. Albedo

[18] Net solar radiation is the most important component of the surface energy budget for alpine glaciers and the amount of insolation available for melting is governed by glacier albedo; thus, an albedo submodel is an important component of the SEBM as demonstrated by *Klok and Oerlemans* [2004]. The albedo submodel used here is empirically based and is similar to that of *Brock et al.*

[2000] except that it computes changes in albedo on arbitrary, instead of daily, timescales. We calculate the broadband albedo of snow (corresponding to our solar radiation measurements) as It decreases from a maximum value of 0.81 (new snow) as a function of cumulative PDDs

$$\alpha_{\text{snow}} = a_{\text{decay}} \ln\left(\sum PDD\right) + \alpha_{\text{fresh}}. \qquad (9)$$

Unrealistically high albedos that are calculated for fractional PDDs are reset to the albedo for fresh snow (α_{fresh}). In this approach, temperatures higher than the melting point act as surrogate for the increase in grain size and liquid water content responsible for lowering the surface albedo [*Wiscombe and Warren*, 1980]. We assume that the subfreezing changes in snow structure occur at a rate that is insignificant relative to the effects of summer meltwater production and changes in snow grain morphology on this temperate glacier. The more detailed grain evolution albedo models also introduce more free parameters into the model. Such models also require quantification of the debris content of the snowpack, which were not measurements made in this study.

[19] A base albedo [*Oerlemans*, 1992] is set as the background albedo of the ice/firn surface and is used when all snow has ablated off of that surface

$$\alpha_{\text{ice}} = a_1 \tan^{-1}\left(\frac{z - z_{\text{ELA}}}{a_2}\right) + a_3. \qquad (10)$$

Equation (10) gives this base albedo and represents a bimodal function with an abrupt increase near the value of z_{ELA} which we set to 1950 m for both ablation seasons. In this function $a_1 - a_4$ are parameters that affect the shape of the transition from low albedo below the ELA to high albedo above; z is elevation; z_{ELA} is the ELA; and α_{ice} is the calculated background albedo. The albedo model keeps track of multiple snowfall layers such that new layers are added when a threshold of 10 or more PDDs have passed between successive snowfalls. The model proved to be insensitive to a range of degree day thresholds from 1 to 10 so a value was chosen to limit the total number of snowfall layers to expedite simulations. The translucency of snow is incorporated to allow surfaces with lower albedos lying below the topmost surface to affect energy absorption at the surface

$$\alpha = \alpha_1 + \exp\left(\frac{-d_{\text{snow}}}{d_0}\right)(\alpha_2 - \alpha_1). \qquad (11)$$

In equation (11), α_1 is the top layer albedo, α_2 is the underlying surface's albedo, d_{snow} is snow depth, d_0 is a reference snow water equivalent depth. A value of 0.025 m WE was chosen for consistency with the range from other studies [*Oerlemans and Knap*, 1998; *Brock et al.*, 2000; *Denby et al.*, 2002; *Willis et al.*, 2002]. For ice, the background albedo is applied, and no temporal variation in ice albedo is incorporated.

2.4.3. Longwave Radiation

[20] Net longwave (wavelengths of $3.5-50~\mu$m) radiation at each model grid point is the sum of incoming and out-

going fluxes that are determined by air temperature, humidity, and topographic features

$$L_{\text{net}} = L_{\downarrow} - L_{\uparrow}. \tag{12}$$

In equation (12), $L_{\downarrow}$ is downwelling longwave, $L_{\uparrow}$ is upwelling longwave, and L_{net} is net longwave. The measured downwelling longwave radiation is adjusted by the ratio of that calculated for the hut to that calculated for the grid cell in question using the relative humidity/emissivity relationship described above and shown in Figure 2. This adjustment incorporates changes in downwelling longwave associated with changes in temperature with elevation. Downwelling longwave radiation at a cell is a combination of the measured value adjusted for elevation and that emitted by surrounding terrain. Longwave emitted by terrain is calculated using the Stephan-Boltzmann relationship with an emissivity of 0.95 (ε_r)

$$L_{\text{terrain}} = \varepsilon_r \sigma T_a^4. \tag{13}$$

The calculation of emission from surrounding terrain, L_{terrain}, relies on near-surface air temperature despite the likelihood that the air temperature at the average emission level of surrounding topography is probably colder. *Plüss and Ohmura* [1997] show that the majority of longwave radiation emitted by a surface is attenuated by the atmosphere within a radius of one half of a kilometer. This suggests that longwave radiation emitted from valley walls 500 m above the glacier will largely combine with the emission from air between the emitting wall and the glacier making the application of air temperature here a reasonable approximation. This effect is also pointed out by *Greuell and Knap* [1997]

$$L_{\downarrow} = L_{\text{inmeas}}(\Phi) + L_{\text{terrain}}(1 - \Phi). \tag{14}$$

The terrain and sky longwave radiation components, L_{inmeas}, are combined using the skyview factor as shown in equation (14). Outgoing longwave radiation from the glacier surface is calculated from the surface temperature using the Stephan-Boltzmann relationship for a blackbody with emissivity of that for ice, $\varepsilon_i = 0.98$

$$L_{\uparrow} = \varepsilon_i \sigma T_s^4. \tag{15}$$

Surface temperature is specified to be at the melting point (273.16 K) when air temperature is above freezing and equal to air temperature when below the melting point. This simplification is made to enable numerous, rapid calculations of seasonal ablation to permit the sensitivity assessment we present here. However, there are impacts with respect to this assumption, and these will be discussed later in section 4.3.

2.4.4. Turbulent Heat Fluxes

[21] Sensible and latent heat fluxes at the glacier surface are computed from a bulk transfer approach. For a stable boundary layer like that which dominates over a melting glacier, we apply Monin-Obukhov similarity theory. Other authors have noted that the underlying assumption of bulk transfer theory (the existence of a constant flux layer above the melting glacier) is not met in typical cases [*Denby and Greuell*, 2000; *Oerlemans and Grisogono*, 2002]. Despite this, good simulations of turbulent heat fluxes have been achieved using Monin-Obukhov theory with reasonable parameter values [*Denby and Greuell*, 2000; *Munro*, 2004]. We also point out that SCG does not demonstrate a persistent katabatic flow with a low-level jet that can be the downfall of application of the MO similarity, so we retain this approach

$$H_l = \rho_{\text{air}} L_{\text{vap}} u A \left(\frac{R}{R^*} \right) \left(\frac{e_a - e_s}{P} \right) \tag{16}$$

$$H_s = \rho_{\text{air}} u A (T_a - T_s). \tag{17}$$

The latent (H_l) and sensible (H_s) heat fluxes are calculated using equations (16) and (17). In equation (16) ρ_{air} is dry air density, u is measured wind speed, L_{vap} is the latent heat of vaporization for water, R is the dry air gas constant, R^* is the gas constant for water vapor, e_a is the vapor pressure at measurement height, e_s is that at the surface (taken as saturation), and P is air pressure. The transfer coefficient A is calculated as follows:

$$A = \left[\frac{k}{\ln\left(\frac{z_i}{z_0}\right) + \Psi(z_i, \lambda)\left(\frac{z_i}{\lambda}\right)} \right]^2, \tag{18}$$

in which k is the unitless von Kármán constant ($k = 0.4$), z_l is the measurements height for wind speed and temperature, z_o is the surface roughness length, Ψ is a unitless stability function, and λ is the Monin-Obukhov length

$$\lambda = \frac{\rho_{\text{air}} C_p u^{*3} \frac{(T_a + T_s)}{2}}{kgH_s}. \tag{19}$$

Equation (19) yields the Monin-Obukhov length. In this equation, C_p is the heat capacity of dry air at constant pressure, u^* is the frictional velocity, and g is gravitational acceleration. The frictional velocity, u*, is calculated from equation (20)

$$u^* = \frac{ku}{\ln\left(\frac{z_i}{z_0}\right) + \Psi(z_i, \lambda)\left(\frac{z_i}{\lambda}\right)}. \tag{20}$$

A consequence of our treatment of surface temperature is that sensible heat flux goes to zero when air temperatures are below the melting point. This situation results in infinite Monin-Obukhov length such that z_i/λ goes to zero yielding a neutrally stable log profile

$$\Psi(z_i, \lambda) = \left\{ \begin{array}{ll} \Psi = 5 & \frac{z_i}{\lambda} > 0 \\ \Psi = 0 & \frac{z_i}{\lambda} \leq 0 \end{array} \right\}. \tag{21}$$

The stability function in equation (21) is used to adjust the log profile used in equations (18) and (20).

[22] Equations (16)–(21) are solved by numerical iteration and, for typical conditions, are convergent (we iterate until λ changes by less than 5% between successive steps). During times of low wind speeds ($u < 2$ m s^{-1}) convergence is slow or unattainable. In those rare cases, wind speed is gradually increased until convergence is achieved. This may lead to a small overestimation of heat flux, but because the lowest converging wind speeds are associated with low fluxes of sensible and latent heat (equations (16) and (17)) the errors incurred from this simplification are small. We have compared this approach to that of disregarding the stability correction and observed a more realistic, continuous function of turbulent heat fluxes with temperature and wind speed using our method.

2.4.5. Temperature Distribution

[23] The temperature field over SCG is thought to be complex along the length of the glacier and laterally. Katabatic flow probably occurs sporadically over all or parts of SCG in summer because of the sloping surface and positive downward sensible heat flux, yet this flow is likely embedded in a larger-scale valley wind regime (SCG heads a deeply incised, valley extending down to 400 m elevation). Lapse rates calculated from temperature data from 2004 and 2005 (Figure 3) show that during warm periods, weak or inverted lapse rates occurred at glacier surface stations. The quality of linear fit of temperature to elevation (R^2; Figure 3) shows that temperatures do not vary coherently with elevation during periods of weak lapse rate. Inspection of individual daily averages reveals that the midlevel temperature logger, P1, was anomalously cold compared to the upper and lower stations indicating presence of cold air drainage at this site. Mean lapse rates for both years were around 6.5°C km^{-1}. These temperature lapse rate fluctuations were modeled with a piecewise-linear relationship between stations, which explicitly accounts for fluctuations in lapse rate along the glacier centerline at hourly timescales. Similar analyses of surface temperature have been performed for the larger Pasterze Glacier, Austria [Greuell and Knap, 1997] where katabatic flow was dominant throughout much of the ablation season. Braun and Hock [2004] report the importance of incorporating a variable lapse rate for simulations of an Antarctic island ice cap.

2.4.6. Precipitation

[24] Precipitation increases with elevation by applying a multiplication factor calculated as a function of vertical distance from the measurement elevation (1580 m in this application)

$$\text{Pre}(z) = \text{Pre}_\text{meas}\left[\Gamma_p \cdot \left(z - z_\text{pre}\right) + 1\right]. \qquad (22)$$

This is analogous to a dimensionless precipitation lapse rate, but scales the enhancement or depletion by the measurement such that a precipitation enhancement or reduction factor is calculated. This method follows that used in the precipitation distribution model described by Daly et al. [1994]. A snowfall threshold of 1°C is used, at or below which precipitation falls as snow. This is a value commonly used [i.e., Arnold et al., 2006], but which also could have an impact on the modeled ablation presented here. Further study would be useful for precisely quantifying this threshold or, more importantly, the spatial-temporal varia-

bility of this threshold. For the time being, we retain the conventional value. The snowpack was initialized at the beginning of simulations using a second-order polynomial in elevation with coefficients determined for each individual year's accumulation measurements.

2.5. Modeling Experiments

[25] There are two goals for our modeling experiments: (1) to achieve the best simulation of SCG ablation during the 2004 and 2005 seasons and (2) to quantify the uncertainty of ablation calculations for SEBMs similar to our model due to uncertainties in physical parameters and input data. The 2004 model runs are from 1 April through 27 October. The 2005 simulations span 11 May through 12 September because of the loss of a wind sensor to winter conditions. Uncertainties are quantified analogously to Murphy et al. [2004] who varied parameters to assess uncertainty in climate change estimates from General Circulation Models. We evaluate model performance by comparing measurements of ablation made during the two ablation seasons with simulated ablation values from the grid node nearest the ablation stakes. The quality of fit is assessed using the root mean square error (RMSE) calculated as

$$\text{RMSE} = \sqrt{\frac{1}{n}\sum_{j=1}^{n}\left(x_{0j} - x_j\right)^2}. \qquad (23)$$

In which n is the number of ablation measurements, x_{0j} is an individual measurement, x_j is the corresponding modeled ablation, and RMSE is the root mean square error. Two steps were used to find the model minima and to assess model error. First, a parameter optimization algorithm (Downhill Simplex [Press et al., 1992]) was used to vary parameters within physically realistic constraints (i.e., positive or negative as needed and within 1 order of magnitude of accepted values) to seek the optimal model fit. Multiple optimization attempts starting with different initial parameter sets were performed to ensure that the resulting minima were global. Identical techniques were used for the 2004 and 2005 simulations.

[26] Second, we analyzed a suite of 10^3 model runs to evaluate the distribution of simulated mass balance over a range of parameter values. Each model run was performed with parameters that were varied randomly by ±5% of the optimized values shown in Table 3. The choice of a 5% range in parameters excludes a large range of physically realistic parameter values. As such, the results of this analysis does not yield a global estimate of the uncertainty in annual net balance. The range was chosen to answer the question of how much variation in model results could be incurred for a fixed amount of uncertainty in physical parameters. For this, 5% was chosen to reflect the parameter ranges commonly assessed in the literature.

[27] Finally, the optimized runs for the complete 2004 ablation season was analyzed for sensitivity to variations in individual parameters and input meteorological data. The parameters were varied about the optimum values at 5% intervals spanning ±10%. The meteorological data were varied by factors of 0.1 over the range 0.8−1.2 times the measured values for all variables except temperature.
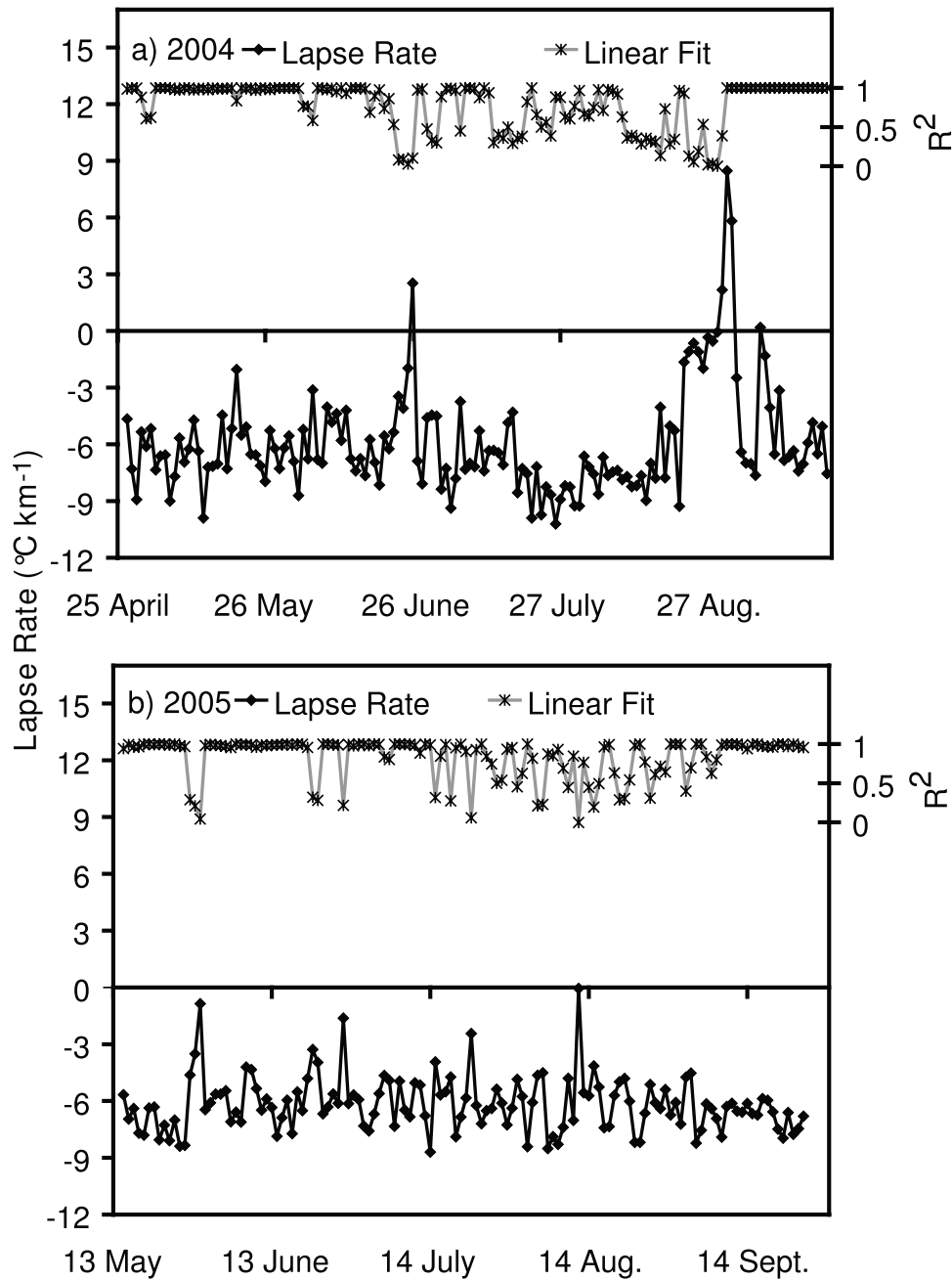
Figure 3. The 2 m air temperature lapse rate (diamonds on black line) for daily mean temperatures along SCG centerline as determined by regression of temperature on elevation for (a) 2004 and (b) 2005. The R^2 is plotted (stars on gray line) as an indication of the quality of a linear model. Periods with less-steep or inverted lapse rates frequently correspond to poor linear fits. The values from late 2004 rely on two stations (thus $R^2 = 1$).

Temperature was varied in half degree increments from $-1.0°C$ to $+1.0°C$. The sensitivity to nighttime and daytime changes was determined by changing temperature in one degree intervals from $-2°C$ to $+2°C$ between the hours of 20:00 to 08:00 for the nighttime experiments and between 08:00 to 20:00 for the daytime experiments. Sensitivity was computed by fitting second-order polynomials to the results for a given variable or parameter and the slope was determined about the origin. This exercise is useful in interpreting the results of the random parameter variation

runs described above. For the meteorological data, this exercise assists in evaluating the sensitivity of estimates of net balance to uncertainties in the measured meteorological data.

3. Results

3.1. Energy Balance Components

[28] The temperate climate of SCG results in high energy fluxes during the ablation season. Summer is characterized

Table 3. Calibrated Model Parameters and Their Sensitivity Compared With Literature Values

Parameter	2004 Value	2005 Value	Representative Literature Ranges	2004 Sensitivity Range	2004 Sensitivity, m WE %$^{-1}$
Γ_p km^{-1}	2.8	3.5	1.0−3.0[a]	2.5−3.1	0.011
z_o Ice mm	44	9.6	0.1−80[b]	43−45	−0.005
z_o Snow mm	4.4	1.7	0.2−30[b]	4.2−4.6	−0.005
ψ	0.62	0.67	0.69−0.76[c]	0.55−0.69	−0.002
$\alpha_{terrain}$	0.20	0.26	0.1 (variable)[d,e]	0.175−0.225	−0.001
a_{decay}	−0.042	−0.038	−0.067 to −0.049[f,g]	−0.046 to −0.038	−0.023

[a]*Daly et al.* [1994].
[b]*Brock et al.* [2006].
[c]*Greuell and Knap* [1997].
[d]*Hock and Holmgren* [2005].
[e]*Tsvetsinkaya et al.* [2002].
[f]*Brock et al.* [2000].
[g]*Pellicciotti* [2004].

by warm temperatures, and long cloud-free periods. Measurements indicate that the 2004 and 2005 ablation seasons generated very negative net balances relative to previous years, and thus should show anomalously high downward energy fluxes. Table 4 presents the monthly mean energy fluxes for a point near the terminus of the glacier for the 2004 and 2005 modeled periods. For both years, net shortwave radiation is the dominant energy source. Higher average shortwave values are evident for 2005, probably because of longer periods of clear weather, less snowfall, and a longer period with low-albedo firn and ice surfaces exposed. Net longwave radiation is upward on average for both years, indicating predominance of clear sky or high cloud conditions. Net longwave radiation is also the smallest magnitude component of the net energy budget, representing 5 and 3% of the total energy in the 2004 and 2005 budgets, respectively. Sensible heating contributed 29% of the total energy budget in 2004 and 24% in 2005 with the flux in 2004 being, on average, 10% greater than that of 2005. Latent heating is similar for both years and the consistently positive downward flux indicates condensing conditions on the glacier.

[29] Time series of hourly energy fluxes for weeklong periods in the beginning of June 2005 (Figure 4a) and in the beginning of August 2005 (Figure 4b) illustrate the short-term, meteorological control on the glacier energy balance. The June period displays overall low energy flux with low net solar radiation, positive longwave radiation flux, and positive latent heat flux suggesting cool, cloudy conditions. In contrast, the August period begins with a so-called rain-on-snow event on 1 August and then displays prevalent summer clear-sky conditions. The rain-on-snow period is

characterized by high fluxes of sensible and latent heat as a result of high winds, warm temperatures, and high humidity. Insolation is low, yet single time step energy flux totals achieve values ~30% higher than during the subsequent clear, calm period. The magnitude of these heat fluxes is comparable to that modeled by *Marks et al.* [1998] and demonstrates that high ablation rates during warm, rainy periods are accounted for by turbulent heat fluxes rather than conductive heat flux from precipitation. Overall, conditions during the clear period show low turbulent heat fluxes due to strongly stable stratification, negative longwave balance, and dominance of the solar radiation flux. After 1 August, clear-sky conditions prevail with high net solar radiation due to the low albedo of the exposed ice surface. Longwave radiation is also important during this period with net upward fluxes of ~50 W m^{-2}.

3.2. The 2004 and 2005 Ablation and Net Balance

[30] The optimized model runs for 2004 and 2005 yield simulated ablation amounts that explain 91 and 93% of the variance in ablation data during the respective years (Figure 5). The RMS error between measured and modeled ablation for 2004 (0.26 m WE) is greater than that of 2005 (0.21 m WE). Least squares estimation of the slope of the line fitting measured and model ablation data yields 0.91 ± 0.08 for 2004 and 0.97 ± 0.05 for 2005. In both years, there is a slight tendency for the model to underestimate higher ablation measurements as evidenced by a least squares fit with slope <1. The majority of underestimated ablation amounts are from the glacier toe where ablation rates are high, especially in 2004. The scatterplots for 2004 also show how well the model accounts for accumulation events

Table 4. Monthly Averaged Energy Balance Components[a]

Averaging Period	S_{net} 2004	S_{net} 2005	L_{net} 2004	L_{net} 2005	H_s 2004	H_s 2005	H_l 2004	H_l 2005	Σ 2004	Σ 2005
April	42	–	−44	–	16	–	−23	–	−9	–
May	50	*46*	−16	*−39*	13	*25*	−1	−9	46	*23*
June	90	101	−18	6	27	31	3	8	100	147
July	159	156	−8	−5	72	56	18	21	241	227
August	112	139	−1	−15	53	44	29	16	193	185
September	56	*78*	−8	*−8*	52	*34*	19	*10*	119	*113*
October	26	–	−17	–	42	–	−4	–	46	–
JJA Means	**120**	**132**	**−9**	**−5**	**51**	**44**	**16**	**15**	**178**	**186**

[a]The italicized entries represent averages over less than a complete month's worth of data for the 2005 simulations. May includes 20 days, and September includes 12 days. The span of simulations is given in the text.
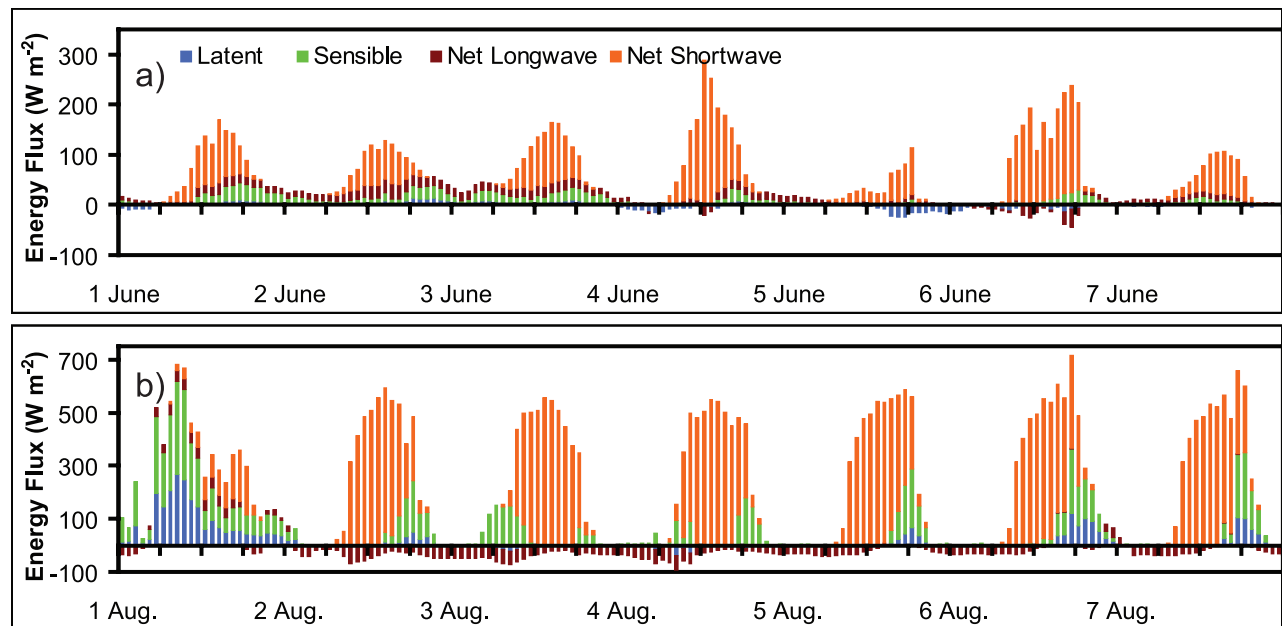
Figure 4. Hourly energy fluxes for a cloudy period in (a) June and (b) early August 2005. The first day in August shows a "rain on snow" event with very high sensible and latent heat fluxes with little radiation input. Note that the energy flux scale is expanded for the June results.

on SCG, with four out of five measurements of net accumulation well simulated.

[31] There is a good fit between modeled ablation and the time series of net balance from the SDS at the glacier AWS for summer 2005 (Figure 6). The simulated net-balance time series at the midglacier site are consistently within a few centimeters of measurements. There is a slight departure in early August during which measured ablation rates are higher than modeled rates. No ablation stake measurements for 2005 indicate accumulation directly, thus failing to provide a direct tuning target for accumulation in the optimization scheme. Comparison of early season modeled accumulation with the SDS records, however, indicates good agreement with measured accumulation events. The integrated effect of accumulation on monthly interval ablation measurements thus provides enough information for the tuning procedure to capture daily temporal details. Ablation at the terminus is also well replicated by the model. Similar to the upper glacier site, modeled early season ablation rates at the terminus are higher than measurements, causing the records to diverge somewhat to a maximum difference of ~30 cm. Late season modeled ablation rates are lower than measurements and thus compensate for higher rates simulated earlier in the season, yielding a final difference between modeled net balance and measurements of only a few centimeters.

[32] Modeled and measured ablation rates in early season, 2005 at the midglacier AWS site are in good agreement with both accumulation and ablation events (Figure 7). The measured average ablation rate is 0.029 m WE d^{-1} whereas the model simulated a value of 0.031 m WE d^{-1}. The higher than measured ablation rate agrees with the change from slightly overestimated specific net balance during early season to an end-of-season value in agreement with ablation stakes. Good performance is expected here because this

AWS provided the temperature, wind speed, and humidity data that drove the 2005 model simulations. Beginning in early August, the correspondence between modeled ablation rates and the rates estimated from the SDS is not quite as good on a daily basis, but multiday average ablation rates remain comparable. The transition from well to poorly modeled daily ablation rates occurs a few days after the change from snow to ice at the AWS site implying that snowmelt is more accurately modeled than icemelt.

[33] At the terminus, the average measured ablation rate of 0.051 m WE d^{-1} is identical to the modeled value of 0.051 m WE d^{-1} within the measurement uncertainty. Daily variability in the record, however, is not well reproduced (Figures 7c and 7d) as reflected in scatterplots with little coherency and a R^2 value of 0.46. Overall, the model captures ablation on monthly timescales, but it does not successfully reproduce daily variability. Because we have temperature control at the terminus, and radiation fluxes should be as well modeled here as at the glacier AWS, the difference between simulated and observed ablation is likely due to inaccuracy of modeled wind speed and/or humidity. Wind speeds are not adjusted when distributed across the glacier, while relative humidity is adjusted on the basis of variations in saturation vapor pressure with altitude. Winds at the glacier toe were observed to be gusty compared to the upper glacier and the terminus is probably influenced by interactions between upslope-directed valley winds and downslope glacier winds. The complex wind field probably contributes to the highly variable measured daily ablation rates. This result is interesting for its implications for applying SEBMs to sites without local wind measurements and implies that while annual ablation can be well simulated, shorter temporal fluctuations could have less than half of their variance explained.
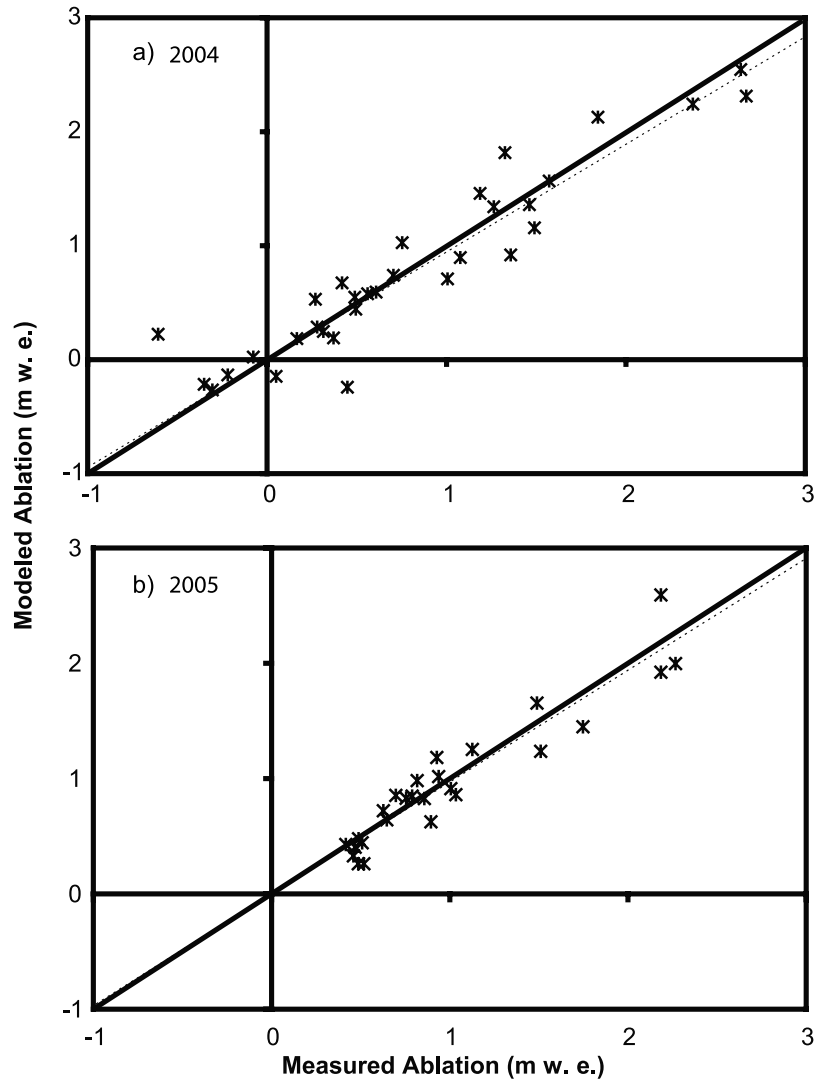
Figure 5. Comparison between measured and modeled ablation for (a) 2004 and (b) 2005. The heavy black 1:1 line is shown. The least squares fit of the data is shown with a light, dashed line. Slopes less than 1 indicate the model's underestimation of ablation with increasing ablation amount.

3.3. Model Sensitivity and Uncertainty

[34] The sensitivity of the model to changes in parameter values reveals which parameters are most influential in determining the observed fluctuations of mass balance during 2004 (Table 3). The parameters governing the elevation gradient of precipitation and the rate of albedo change with aging dominate control over the modeled mass balance, whereas those governing the reflectivity of surrounding terrain and the atmospheric transmissivity are least influential. Transmissivity is only used to calculate potential radiation for comparison to measurements as a surrogate for cloud cover. If this parameter were used directly in the calculation of solar input to the glacier, it would have a much greater influence on the simulated glacier net balance. Scatterplots of net balance and RMSE reveal the best fit model result as well as the nature of the approach to the minima representing the best model (Figure 8). Both years display well-defined roughly parabolic approaches to the minimum RMSE, although optimization takes place over a

six-dimensional parameter space, implying that the curvature is probably more complex than shown here.

[35] The 10^3 realizations about the optimized parameter sets indicated in Figure 8 were used to calculate an error estimate on the computed net mass balance. For both years, the random parameter selection yields an almost normal distribution about the mean, best estimate mass balance value (Figure 9). The net balance simulated for a single run using the best fit set of parameters is chosen as the best model estimate of the net mass balance for the year. These are −1.69 m WE and −2.09 m WE for 2004 and 2005, respectively. Error in these estimates is taken as two standard deviations in the fitted normal distribution for each year's suite of simulations yielding ±0.15 m WE and ±0.07 m WE for the respective years.

[36] The sensitivity of the SEBM to the values of the input meteorological data is presented in Table 5. The sensitivity for temperature is expressed in the conventional m WE per degree as well as the sensitivity per % derived using the absolute Kelvin scale for intercomparison. For the
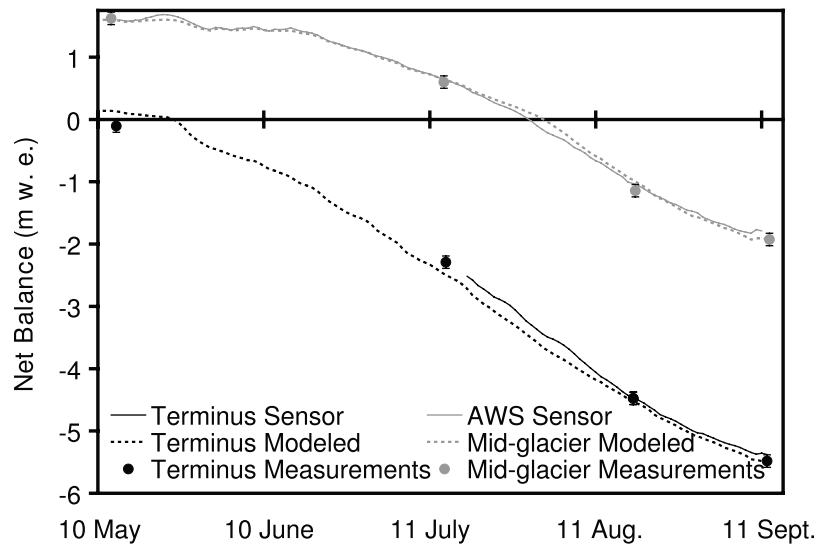
Figure 6. Daily point net balance at the glacier AWS (gray line; denoted midglacier) and at the terminus (black line; denoted terminus) site during 2005. Measurements from the SDS are solid, while the model data are dashed. Ablation stake measurements are indicated with like colored circles. Error bars are ±0.1 m WE uncertainties in ablation stake measurements.
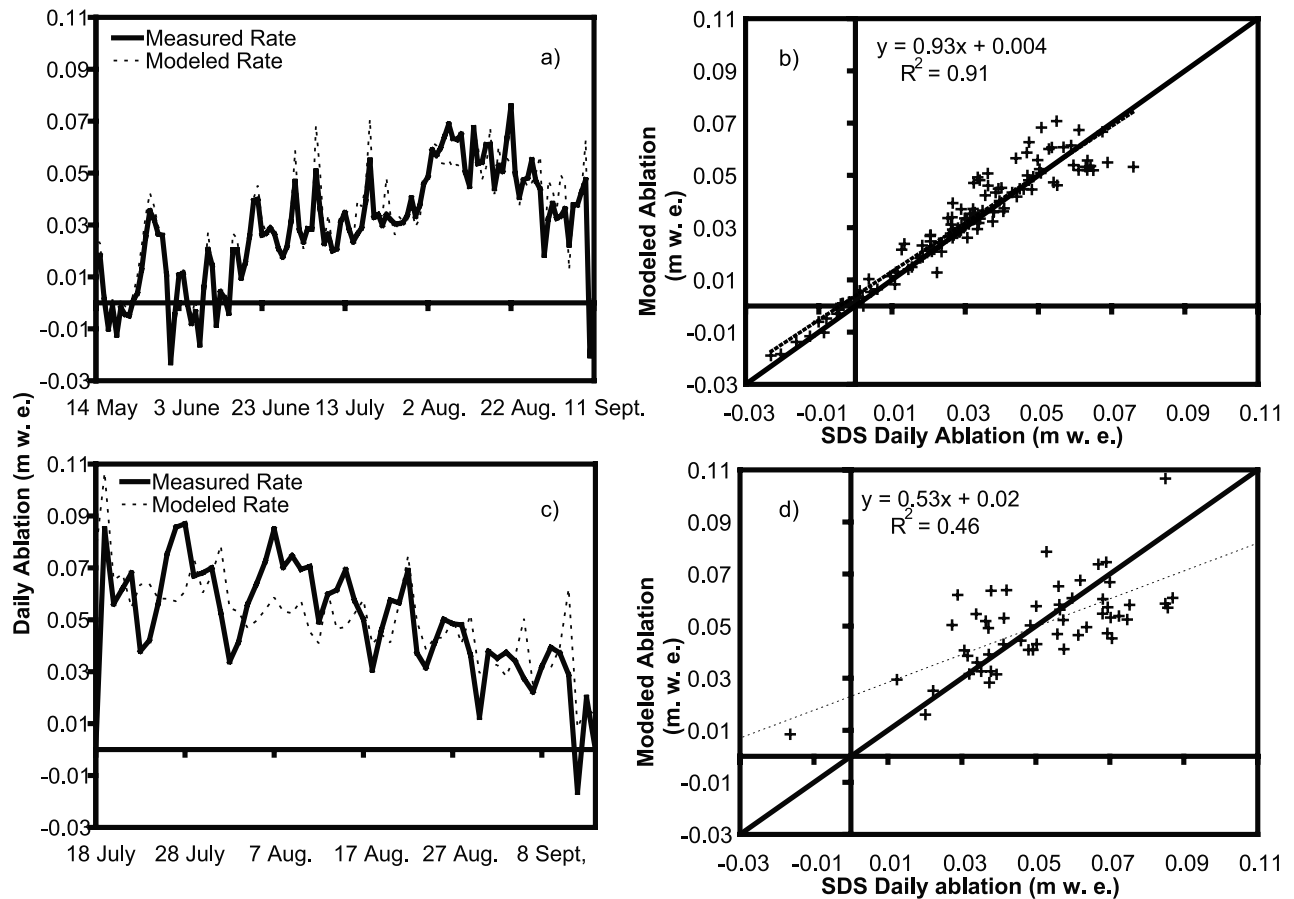
Figure 7. Daily ablation rates from the model (dashed lines) and SDS (solid lines). (a) Time series of results from the glacier AWS, (b) measured versus modeled ablation rates for glacier AWS, (c) results from terminus, and (d) measured versus modeled ablation rates for the terminus. Dashed lines in Figures 7b and 7d are best fit lines, while the heavy, black line denotes a 1:1 relationship.
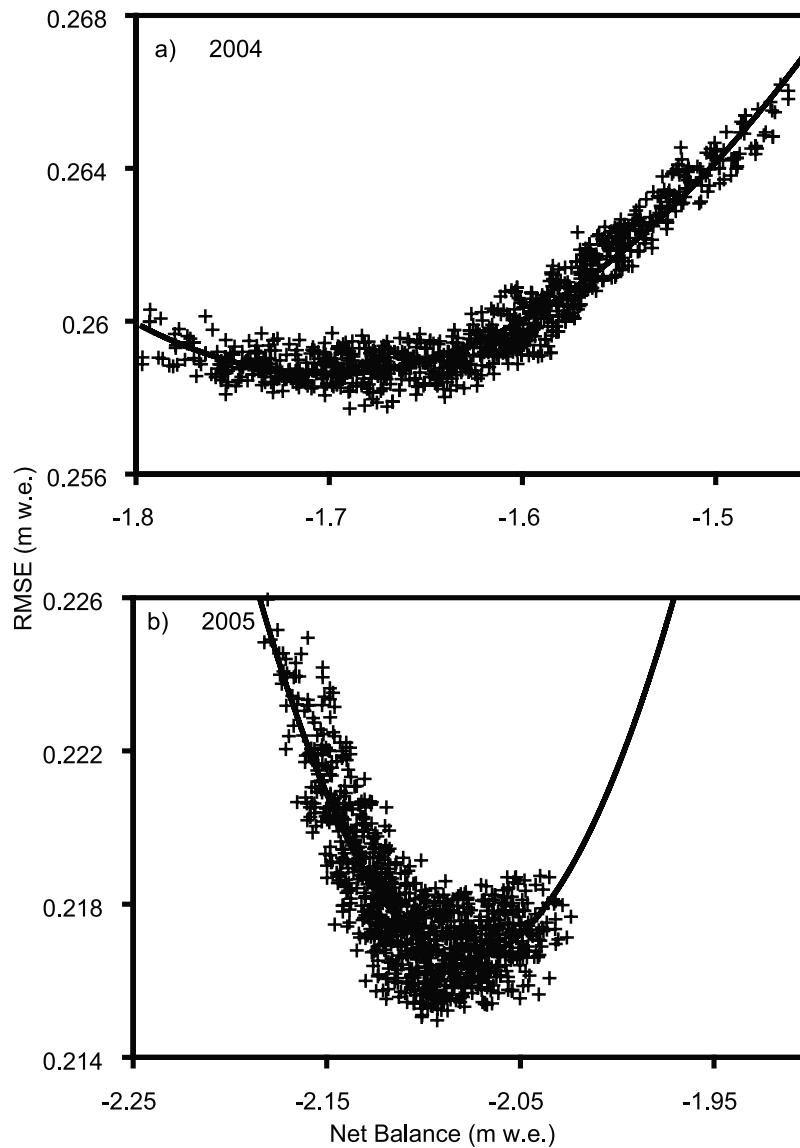
Figure 8. Scatterplot of net balance and RMSE results for the 10^3 model realizations for (a) 2004 and (b) 2005. A second-order polynomial is fit to the data as a guide. The scatter in 2005 results is less than that for 2004, but the scale is kept constant between Figures 8a and 8b.

latter, changes of one to two percent result in large differences in the modeled net balance, but such large changes (2.7–5.4°C) are unexpected with respect to the measurement uncertainty for temperature (see Table 1). The sharp sensitivity to temperature does reflect the importance of temperature changes to summer ablation. The influence of temperature changes taking place during night or daytime only is expressed in Table 5 as well. Net balance is 1.9 times more sensitive to daytime changes than nighttime. The net energy budget is small or negative at night because of longwave radiative cooling, so increases in air temperature still yield a negative energy budget, thereby muting the effect of the perturbation. Altering the longwave has the second greatest influence on ablation. While the overall effect of increasing or decreasing summertime precipitation is small, the value is greater than the direct change in mass flux. For example, for a decrease in summer precipitation of 20%, 18 cm of precipitation are lost while the net balance

decreases from −1.69 m WE to −2.18 m WE This change represents an enhancement of ∼2.6 times the direct contribution roughly half of which is due to amplification by the precipitation lapse rate. A strong signal remains, which outlines the importance of summer snowfalls on the net balance of the glacier. Changes in humidity change the net balance as well by increasing the amount of condensation or evaporation. The effect would probably be larger if incoming longwave radiation were recalculated to reflect changes in atmospheric emissivity due to changes in moisture content. Finally, increased wind speed causes increased turbulent exchange. Because the turbulent heat fluxes are dominantly positive, increased winds correspond to increased ablation.

[37] The sensitivity characteristics of the model to input data can be used to estimate the uncertainty in our modeling due to the uncertainty in the meteorological data. We multiply the model sensitivity to input data with the instrument precision associated with the measurements to
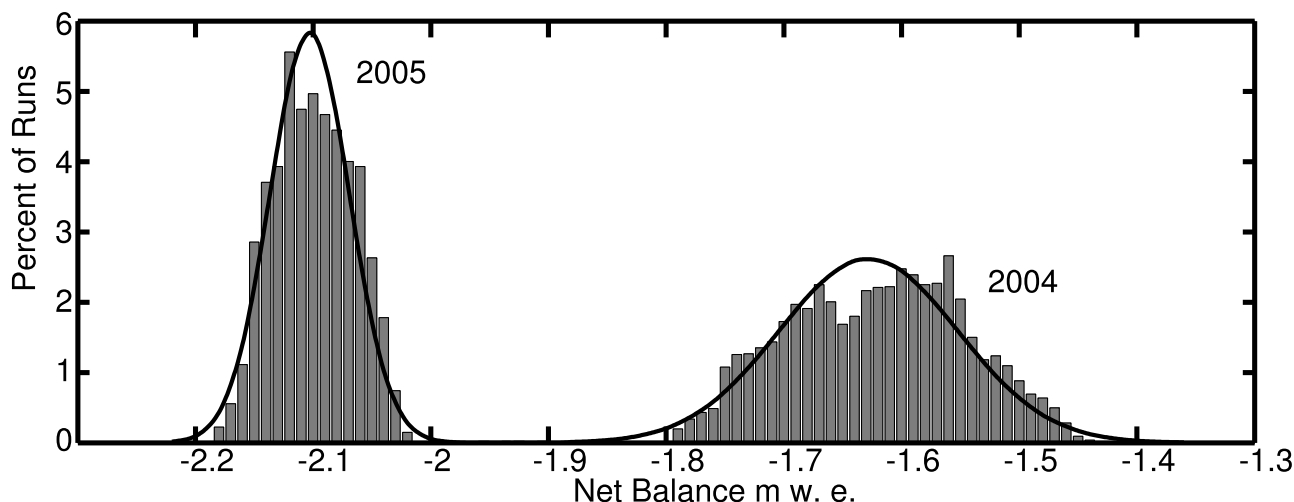
Figure 9. Net balance distributions for the 10^3 simulations of the 2004 and 2005 ablation seasons. The normal distribution fitted to the data is shown by the black curve, while histograms in 0.1 m WE intervals are presented by gray bars.

calculate the uncertainty in the model estimate of ablation. The uncertainties associated with each instrument are combined using the root sum of squared error. For the net balance estimate for 2004, the resulting uncertainty due to instrument error is ±0.23 m WE This yields a total uncertainty in the model estimate of net balance for that year of ±0.38 m WE With the combined uncertainty due to parameters and input data our calculated net balance for 2004 is −1.69 ± 0.38 m WE compared with the measured net balance of −1.74 ± 0.1 m WE For 2005, if we assume a similar uncertainty due to input data, we simulate an 11 September net balance of −2.10 ± 0.30 m WE.

4. Discussion

4.1. Optimized Parameters and Energy Fluxes

[38] Evaluation of the physical parameters optimized by our scheme in relation to literature values is useful for determining the optimization scheme's ability to replicate realistic physical boundary conditions. The exercise is also indicative of an individual year's set of physical conditions. It must be stated, however, that the approach used here cannot be interpreted as an inversion for the "real" values of model parameters; rather, it is instructive to view the estimated parameters as one likely set of boundary conditions for the model. We do not simulate time-varying parameters although surface roughness, surrounding topography albedo, and atmospheric transmissivity are surely time dependent although inroads toward calculating time varying parameters have been made recently [*Brock et al.*, 2000, 2006; *Hock and Holmgren*, 2005].

[39] The best fitting parameter sets are presented in Table 3 along with comparisons with a range of literature values. Generally, the parameter set falls within the range of published values yielding a physically reasonable model. The only major (in terms of influence of modeled net balance) outliers are the precipitation lapse rate determined for 2005 and the snow aging parameter determined for both years, which are discussed below.

[40] The precipitation lapse rates are steep for both years relative to those used in the precipitation distribution model described by *Daly et al.* [1994], whose maximum of 3.0 km^{-1} was used as a limiting value in the Pacific Northwest. Our values of 2.8 km^{-1} and 3.5 km^{-1} are only representative of the summertime simulation period, while the literature values are based on longer-term averages which incorporate winter precipitation. Further, the scale of analysis for our result and the published result is different, and it is conceivable that such sharp precipitation gradients exist on short spatial scales in steep terrain. The precipitation lapse rates used here may also be partially accommodating wind redistribution of snow falls, which may act to increase snow depth on the upper reaches of the glacier is it is in the lee of the dominant SW storm winds. The strong increase in precipitation with elevation agrees with the observed relationship between accumulation at the toe of SCG and that at the upper glacier, which can be a factor of four greater over an elevation span of only 500 m. This is an indication of the complexity of precipitation/snowfall patterns in mountainous terrain.

[41] Our snow aging parameters for both years yield late season snow albedos of 0.52 (2004) and 0.55 (2005), while those by *Brock et al.* [2000] give an albedo of 0.45 for the same number of PDDs. This suggests either that aged snow on SCG is more reflective than that of other alpine glaciers, or the tuning procedure has partitioned energy away from

Table 5. Model Sensitivity to Secular Changes in Input Meteorological Variables

Meteorological Variable	2004 Sensitivity
T	−0.86 m WE °C^{-1}
T_{day}	−1.15 m WE °C^{-1}
T_{night}	−0.60 m WE °C^{-1}
T	−2.15 m WE %$^{-1}$
RH	−0.04 m WE %$^{-1}$
G_{meas}	−0.06 m WE %$^{-1}$
L_{in}	−0.16 m WE %$^{-1}$
u	−0.05 m WE %$^{-1}$
P	+0.02 m WE %$^{-1}$

solar radiation contributions. We have no albedo measurements to confirm or refute the former possibility, but the modeled albedos are reasonable to high for an alpine glacier [*Klok and Oerlemans*, 2004]. As for the second possibility, the surface roughness lengths determined for both years are high, suggesting that the latter case may be correct. We also discuss below the possibility that high albedo might serve to compensate for our parameterization of surface temperature.

[42] The surface roughness lengths used in the best fit models are on par with, or somewhat higher than, values in the literature. The high ends of the values quoted in the literature are for unusually rough/crevassed glacier surfaces. Typical z_0 for snow is ∼2 mm and for ice is 2–10 mm [*Brock et al.*, 2006]. Ice on SCG is typically more heavily crevassed than snow and is hummocky at length scales of 1–2 m, so larger roughness lengths are expected here. However, a value of 44 mm is comparable to the largest roughness lengths published, which are for hummocky ice in Greenland [*Smeets et al.*, 1999]. As we suggest in section 3.2, ablation modeled on the glacier terminus is subject to uncertainties in wind speed there. If wind speed is underestimated at the terminus, then the surface roughness for ice would be adjusted upward to compensate.

[43] The albedo of surrounding terrain and the atmosphere's transmissivity both wield the least influence on ablation. The difference between the 2004 and 2005 optimized values of transmissivity amount to an ablation difference of 0.02 m WE between the years. The value optimized for atmospheric transmissivity is below that typical for clean-air and clear-sky conditions. However, the low sensitivity of the model to this parameter allows this variable to be changed by 10% to more reasonable values around 0.75 with only a 0.02 m WE change in the modeled ablation for 2004. The difference between optimized values of the albedo of surrounding terrain yields a small (0.03 m WE) difference between the years. The low sensitivity of the model to the albedo of surrounding terrain implies that the reflectivity of the basin is of little importance as incorporated in this model. Measurements of incoming solar radiation typically peak in the spring before summer solstice, and we infer this peak to be a result of the snow covered surrounding topography. These high radiation values are offset by the high albedo of the glacier at this time, but are probably important for initializing the melt season.

[44] The SEBM sensitivity to variations in the input meteorological data shows that incoming longwave radiation has the greatest influence on ablation rates in spite of the low contribution of net longwave to the total energy budget. The sensitivity to incoming longwave radiation is roughly 2.7 times greater than for incoming solar radiation in a glacier-wide sense. The absorption of longwave is fairly uniform across the glacier in space and time, whereas variations in incoming solar radiation will have the largest effect near the terminus where albedo is low. This result underscores the arguments of *Ohmura* [2001] who suggests that longwave input is an important justification for ablation models based primarily on air temperature. Wind speed also has a large effect on the net balance, which supports the conclusion that the model's failure to capture the day-to-day variability in ablation at the terminus is likely due to inaccuracies in wind speeds applied there. The overall model sensitivity to input data is roughly twice the model's sensitivity to physical parameters, but both are significant. Overall, this suggests that equal efforts be put into improving input data fields as well as the physical parameters used in SEBMs.

4.2. Optimization and Monte Carlo Error Estimates

[45] The optimization scheme was able to seek out a robust estimate of the parameters chosen for variation in this work, and the derived parameters are within the physical estimates presented in the literature. Since multiple search start points were used to initialize the downhill simplex method, it is likely that an approximate minimum was found and that it was global. The Monte Carlo assessment yields a large spread for a small range in physical parameters, which underscores the importance of feedbacks between physical processes operating in the model. The statistical distribution of modeled net balance is probably a minimum spread since surface roughness lengths, for example, could range over 1 order of magnitude rather than the ±5% used here between all parameters for consistency. With a given set of parameters applied to a longer temporal simulation of glacier net balance, even a small over or underestimation could accumulate into large errors in cumulative net balance.

4.3. Impacts of Simplifying Surface Temperature

[46] We have chosen to simplify our SEBM by stipulating that there is no subsurface heat flux in the glacier, and by pinning T_s to air temperature when freezing conditions occur. This assumption could be incorrect when the surface energy balance falls below zero when measured air temperatures are above the melting point, and also when air temperatures fall below freezing and snow or ice at the melting point will release energy to the atmosphere. These inconsistencies will have impacts on the flux of upwelling longwave energy as well as the turbulent heat fluxes. However, this simplification is commonly made including in this work, which warrants discussion and quantification of the impacts.

[47] In our current simulations, when the surface energy balance is negative, the average flux is −32 W m^{-2}, and this occurs during roughly half of the nights in 2004 and one third of nights in 2005. This flux should be accommodated by cooling the snow or ice surface, or by refreezing liquid water in the snowpack or liquid surface water on ice. If we assume that the top ∼20 cm of snow takes part in the diurnal cycle and a liquid water fraction of 0.03, then ∼1 MJ m^{-2} of energy are required to freeze all of the water in that layer. At our modeled average negative flux for 2004, 10 h are required to provide enough cooling, and a similar period is required to refreeze a plausible 0.5 cm thick free water layer on ice. During this period, the surface temperature will remain at the melting point, so the temperature approximation used here is likely accurate. However, in order to begin to effectively remove mass from the glacier when the energy balance becomes positive, the material that refroze during the night needs to be remelted, requiring that the 1 MJ m^{-2} of energy that was invested to refreeze surface water will be required of the positive energy flux before melt occurs.

[48] *Klok and Oerlemans* [2002] explicitly calculate surface temperature using a two layer heat flux scheme, and

this approach will yield good results when free water has already frozen. Our above calculation, however, shows that for conditions present on SCG, this situation will rarely be met. If *Klok and Oerlemans*' [2002] approach were to be applied, cooling of the surface temperature would be simulated, and the sensible and latent heat and upwelling longwave fluxes would be too small in magnitude. We can easily quantify the change in upwelling longwave if we again assume the upper 20 cm of the snow is diurnally active, our late season snow density of 530 kg m^{-3}, and a specific heat capacity of ice of 2097 J kg^{-1} K^{-1}. With 10 h of cooling at 30 W m^{-2} the surface temperature could cool as much as 5 K resulting in an upwelling longwave radiation flux that is 22 W m^{-2} less than if the surface remained at the melting point. For ice the compensation will be 12 W m^{-2} because of the increased density. These fluxes partially offset the errors in the surface energy flux that are accrued by keeping the surface temperature fixed at the melting point. Excessively cold surface temperatures will also lead to greater stability in the boundary layer and suppression of latent and sensible exchange. However, in our simulations nighttime turbulent fluxes during negative energy budget periods are already small, so the impact on these should be minimal.

[49] It bears stating that the subsurface temperature calculations of *Klok and Oerlemans* [2002] are important for accounting for energy storage and release in the glacier on diurnal and seasonal timescales. Because of these processes, both refreezing in the snowpack and surface cooling should be explicitly calculated in SEBMs. This conclusion was reached by *Fierz et al.* [2003] for snow energy balance models. Over the relatively small spatial scales that SEBMs for alpine glaciers are applied, a detailed subsurface heat flux calculation would not be too computationally expensive. The CROCUS model *Brun et al.* [1989] applied to Glacier de Saint Sorlin and Glacier d'Argentière by *Gerbaux et al.* [2005] incorporates a detailed subsurface energy and mass flux model. A level of complexity intermediate between two-layer models and CROCUS is probably most appropriate. Because our approach does not account for the negative energy fluxes, the result is an effective increase in the time averaged energy flux to the glacier. In the energy balance calculations presented here it is speculated that the potentially "too high" albedo discussed above might be compensating for this effect to yield a good fit to measured ablation data.

5. Conclusion

[50] A surface energy balance model has been developed and applied to South Cascade Glacier over the 2004 and 2005 ablation seasons. The model utilizes physical parameterizations of the most important energy transfer processes to compute ablation and includes detailed temperature, humidity, and radiation distribution across the glacier. The model is first tuned to SCG by altering six physical parameters not measured in the field program. We then estimated the uncertainty in the model calculation of net balance by performing 10^3 simulations with simultaneous random variations of the parameters mentioned above about a range of ±5% of the optimum value. We also combine model sensitivity to input meteorological data with rated instrument error to fully describe the range of the SEBMs

uncertainty. For 2004, a net mass balance of −1.69 ± 0.38 m WE was computed for the period ending 30 September and is 0.04 m WE greater than the measured water year net balance. Of the reported 2004 ablation season uncertainty, 0.23 m WE are due to uncertainty in the input data, while 0.15 m WE are due to parameter uncertainty indicating that parameter uncertainty is of equal magnitude to that because of uncertainties in meteorological measurements. For 2005 as of 11 September a balance of −2.10 ± 0.30 m WE was reached, which is within 0.42 m WE of the reported water year balance, with 19 d remaining in the ablation season.

[51] With respect to physical parameters the greatest sensitivity of the SEBM presented here is to the parameters governing precipitation distribution and the snow aging parameter used to calculate albedo. The SEBM's sensitivity to variations in input meteorological data show that incoming longwave radiation has the greatest weight in the net balance outcome. The affect of uncertainty in precipitation is small compared with the other variables, but the magnitude of changes is amplified through albedo feedbacks on the glacier by a factor of 2.6. The sensitivity of ablation to temperature is −0.86 m WE °C^{-1} and is greater during day than during night by a factor of 1.9.

[52] Overall, the combination of energy balance modeling with Monte Carlo estimation of model uncertainty is a powerful tool for judging uncertainty in model results and comparing model results with measurements. This method is easily applied and would be useful to consider in larger temporal and spatial scale applications. Specifically, this technique should be applied to simulations of glacier mass balance in past or future climates where physical parameters are strictly not easily characterized.

References

Arendt, A. A., K. A. Echelmeyer, W. D. Harrison, C. S. Lingle, and V. B. Valentine (2002), Rapid wastage of Alaska glaciers and their contribution to rising sea level, *Science*, *297*, 382–386, doi:10.1126/science.1072497.

Arnold, N. S., I. C. Willis, M. J. Sharp, K. S. Richards, and W. J. Lawson (1996), A distributed surface energy-balance model for a small valley glacier. part I: Development and testing for Haut Glacier d'Arolla, Valais, Switzerland, *J. Glaciol.*, *42*, 77–89.

Arnold, N. S., W. G. Rees, A. J. Hodson, and J. Kohler (2006), Topographic controls on surface energy balance of a high arctic valley glacier, *J. Geophys. Res.*, *111*, F02011, doi:10.1029/2005JF000426.

Bidlake, W. R., E. G. Josberger, and M. E. Savoca (2007), Water, ice, and meteorological measurements at South Cascade Glacier, Washington, balance years 2004 and 2005, *U.S. Geol. Surv. Sci. Invest. Rep. 2007-5055*, 38 pp., U.S. Geol. Surv., Reston, Va.

Bougamont, M., J. L. Bamber, J. K. Ridley, R. M. Gladstone, W. Greuell, E. Hanna, A. J. Payne, and I. Rutt (2007), Impacts of model physics on estimating the surface mass balance of the Greenland ice sheet, *Geophys. Res. Lett.*, *34*, L17501, doi:10.1029/2007GL030700.

Braithwaite, R. J. (1981), On glacier energy balance, ablation, and air temperature, *J. Glaciol.*, *27*, 381–391.

Braithwaite, R. J., T. Konzelmann, C. Marty, and O. B. Olesen (1998), Errors in daily ablation measurements in northern Greenland, 1993–1994, and their implications for glacier climate studies, *J. Glaciol.*, *44*, 583–588.

Braun, M., and R. Hock (2004), Spatially distributed surface energy balance and ablation modeling on the ice cap of King George Island (Antarctica), *Global Planet. Change*, *42*, 45–58, doi:10.1016/j.gloplacha.2003.11.010.

Brock, B. W., and N. S. Arnold (2000), A spreadsheet-based (Microsoft Excel) point surface energy balance model for glacier and snow melt

studies, *Earth Surf. Processes Landforms*, 25, 649–658, doi:10.1002/1096-9837(200006)25:6<649::AID-ESP97>3.0.CO;2-U.

Brock, B. W., I. C. Willis, and M. J. Sharp (2000), Measurement and parameterization of albedo variations at Haut Glacier d'Arolla, Switzerland, *J. Glaciol.*, 46, 675–688, doi:10.3189/172756500781832675.

Brock, B. W., I. C. Willis, and M. J. Sharp (2006), Measurement and parameterization of aerodynamic roughness length variations at Haut Glacier d'Arolla, Switzerland, *J. Glaciol.*, 52, 281–297, doi:10.3189/172756506781828746.

Brun, E., E. Martin, V. Simon, C. Gendre, and C. Coléou (1989), An energy and mass model of snow cover suitable for operational avalanche forecasting, *J. Glaciol.*, 38, 13–22.

Brutsaert, W. (1975), On a derivable formula for long-wave radiation from clear skies, *Water Resour. Res.*, 11, 742–744, doi:10.1029/WR011i005p00742.

Collares-Pereira, M., and A. Rabl (1979), The average distribution of solar radiation-correlations between diffuse and hemispherical and between daily and hourly insolation values, *Sol. Energy*, 22, 155–164, doi:10.1016/0038-092X(79)90100-2.

Daly, C., R. P. Neilson, and D. L. Phillips (1994), A statistical-topographic model for mapping climatological precipitation over mountainous terrain, *J. Appl. Meteorol.*, 33, 140–158, doi:10.1175/1520-0450(1994)033<0140:ASTMFM>2.0.CO;2.

Denby, B., and W. Greuell (2000), The use of bulk and profile methods for determining surface heat fluxes in the presence of glacier winds, *J. Glaciol.*, 46, 445–452, doi:10.3189/172756500781833124.

Denby, B., W. Greuell, and J. Oerlemans (2002), Simulating the Greenland atmospheric boundary layer: part II. Energy balance and climate sensitivity, *Tellus Ser. A*, 54, 529–541.

Dozier, J., and J. Frew (1990), Rapid calculation of terrain parameters for radiation modeling from digital elevation data, *IEEE Trans. Geosci. Remote Sens.*, 28, 963–969, doi:10.1109/36.58986.

Dyurgerov, W. (2003), Mountain and subpolar glaciers show an increase in sensitivity to climate warming and intensification of the water cycle, *J. Hydrol.*, 282, 164–176, doi:10.1016/S0022-1694(03)00254-3.

Escher-Vetter, H. (1985), Energy balance calculations for the ablation period 1982 at Vernagtferner, Oetzal Alps, *Ann. Glaciol.*, 6, 158–160.

Fierz, C., P. Riber, E. E. Adams, A. R. Curran, P. M. B. Föhn, M. Lehning, and C. Plüss (2003), Evaluation of snow-surface energy balance models in alpine terrain, *J. Hydrol.*, 282, 76–94, doi:10.1016/S0022-1694(03)00255-5.

Gerbaux, M., C. Genthon, P. Etchevers, C. Vincent, and J. P. Dedieu (2005), Surface mass balance of glaciers in the French Alps: Distributed modeling and sensitivity to climate change, *J. Glaciol.*, 51, 561–572, doi:10.3189/172756505781829133.

Greuell, W., and W. H. Knap (1997), Elevational changes in meteorological variables along a midlatitude glacier during summer, *J. Geophys. Res.*, 102, 25,941–25,954, doi:10.1029/97JD02083.

Greuell, W., and T. Konzelmann (1994), Numerical modeling of the energy balance and the englacial temperature of the Greenland Ice Sheet: Calculations for the ETH-Camp location (West Greenland, 1155 m a.s.l.), *Global Planet. Change*, 9, 91–114, doi:10.1016/0921-8181(94)90010-8.

Hock, R. (1999), A distributed temperature-index ice- and snowmelt model including potential direct solar radiation, *J. Glaciol.*, 45, 101–111.

Hock, R., and B. Holmgren (2005), A distributed energy-balance model for complex topography and its application to Storglaciären, Sweden, *J. Glaciol.*, 51, 25–36, doi:10.3189/172756505781829566.

Iqbal, M. (1983), *An Introduction to Solar Radiation*, 390 pp., Academic, London.

Kaser, G., J. G. Cogley, M. B. Dyurgerov, M. F. Meier, and A. Ohmura (2006), Mass balance of glaciers and ice caps: Consensus estimates for 1961–2004, *Geophys. Res. Lett.*, 33, L19501, doi:10.1029/2006GL027511.

Klok, E. J., and J. Oerlemans (2002), Model study of the spatial distribution of the energy balance of Morteratschgletscher, Switzerland, *J. Glaciol.*, 48, 505–518, doi:10.3189/172756502781831133.

Klok, E. J., and J. Oerlemans (2004), Modelled climate sensitivity of the mass balance of Morteratschgletscher and its dependence on albedo parameterization, *Int. J. Climatol.*, 24, 231–245, doi:10.1002/joc.994.

Klok, E. J., M. Nolan, and M. R. Van Den Broeke (2005), Analysis of meteorological data and the surface energy balance of McCall Glacier, Alaska, USA, *J. Glaciol.*, 51, 451–461, doi:10.3189/172756505781829241.

Konzelmann, T., R. Van de Wal, W. Greuell, R. Bintanja, E. Henneken, and A. Abe-Ouchi (1994), Parameterization of short- and longwave incoming radiation for the Greenland Ice Sheet, *Global Planet. Change*, 9, 143–164, doi:10.1016/0921-8181(94)90013-2.

Krimmel, R. M. (2002), Water, ice, and meteorological measurements at South Cascade Glacier, Washington, 2000–2001 balance years, *U.S. Geol. Surv. Water Resour. Invest. Rep. 02-4165*, 63 pp., U.S. Geol. Surv., Reston, Va.

Laabs, B. J. C., M. A. Plummer, and D. M. Mickelson (2006), Climate during the last glacial maximum in the Wasatch and southern Uinta Mountains inferred from glacier modeling, *Geomorphology*, 75, 300–317, doi:10.1016/j.geomorph.2005.07.026.

Marks, D., and J. Dozier (1992), Climate and energy exchange at the snow surface in the Alpine Region of the Sierra Nevada: 2. Snow cover energy balance, *Water Resour. Res.*, 28, 3043–3054.

Marks, D., J. Kimball, D. Tingey, and T. Link (1998), The sensitivity of snowmelt processes to climate conditions and forest cover during rain-on-snow: A case study of the 1996 Pacific Northwest flood, *Hydrol. Processes*, 12, 1569–1587, doi:10.1002/(SICI)1099-1085(199808/09)12:10/11<1569::AID-HYP682>3.0.CO;2-L.

Meier, M. F. (1958), Research on South Cascade Glacier, *Mountaineer*, 51, 40–47.

Munro, D. S. (1990), Comparison of melt energy computations and ablatometer measurements on melting ice and snow, *Arct. Alp. Res.*, 22, 153–162, doi:10.2307/1551300.

Munro, D. S. (2004), Revisiting bulk heat transfer on Peyto Glacier, Alberta, Canada, in light of the OG parameterization, *J. Glaciol.*, 50, 590–600, doi:10.3189/172756504781829819.

Murphy, J. M., D. M. Sexton, D. N. Barnett, G. S. Jones, M. J. Webb, M. Collins, and D. A. Stainforth (2004), Quantification of modelling uncertainties in a large ensemble of climate change simulations, *Nature*, 430, 768–771, doi:10.1038/nature02771.

Oerlemans, J. (1992), Climate sensitivity of glaciers in southern Norway: Application of an energy-balance model to Nigardsbreen, Hellstugubreen and Alfotbreen, *J. Glaciol.*, 38, 223–232.

Oerlemans, J., and B. Grisogono (2002), Glacier winds and parameterization of the related surface heat fluxes, *Tellus Ser. A*, 54, 440–452.

Oerlemans, J., and N. C. Hoogendoorn (1989), Mass balance gradients and climatic change, *J. Glaciol.*, 35, 399–405.

Oerlemans, J., and W. H. Knap (1998), A 1 year record of global radiation and albedo in the ablation zone of Morteratschgletscher, Switzerland, *J. Glaciol.*, 44, 231–238.

Ohmura, A. (2001), Physical basis for the temperature-based melt-index method, *J. Appl. Meteorol.*, 40, 753–761, doi:10.1175/1520-0450(2001)040<0753:PBFTTB>2.0.CO;2.

Østrem, G., and N. Haakensen (1999), Map comparison or traditional mass-balance measurements: which method is better?, *Geogr. Ann. Ser. A*, 81, 703–711, doi:10.1111/j.0435-3676.1999.00098.x.

Pellicciotti, F. (2004), Development of an ice and snow melt model for long-term analysis of water resources from highly glacierized basins, Ph.D. thesis, 176 pp., Eidg. Tech. Hochsch., Zürich, Switzerland.

Pellicciotti, F., B. Brock, U. Strasser, P. Burlando, M. Funk, and J. Corripio (2005), An enhanced temperature-index glacier melt model including the shortwave radiation balance: Development and testing for Haut Glacier d'Arolla, Switzerland, *J. Glaciol.*, 51, 573–587, doi:10.3189/172756505781829124.

Plummer, M. A., and F. M. Phillips (2003), A 2-D numerical model of snow/ice energy balance and ice flow for paleoclimatic interpretation of glacial geomorphic features, *Quat. Sci. Rev.*, 22, 1389–1406.

Plüss, C., and A. Ohmura (1997), Longwave radiation on snow-covered mountainous surfaces, *J. Appl. Meteorol.*, 36, 818–824.

Press, W. H., S. A. Teukolsky, W. T. Vetterling, and B. P. Flannery (1992), *Numerical Recipes in Fortran 77: The Art of Scientific Computing*, 933 pp., Cambridge Univ. Press, Cambridge, Mass.

Smeets, C. J. P. P., P. G. Duynkerke, and H. F. Vugts (1999), Observed wind profiles and turbulenc fluxes over an ice surface with changing surface roughness, *Boundary Layer Meteorol.*, 92, 101–123.

Tsvetsinkaya, E. A., C. B. Schaaf, F. Gao, A. H. Strahler, R. E. Dickinson, X. Zeng, and W. Lucht (2002), Relating MODIS-derived surface albedo to soils and rock types over Northern Africa and the Arabian peninsula, *Geophys. Res. Lett.*, 29(9), 1353, doi:10.1029/2001GL014096.

Walraven, R. (1978), Calculating the position of the sun, *Sol. Energy*, 20, 393–397, doi:10.1016/0038-092X(78)90155-X.

Willis, I. C., N. S. Arnold, and B. W. Brock (2002), Effect of snowpack removal on energy balance, melt and runoff in a small supraglacial catchment, *Hydrol. Processes*, 16, 2721–2749, doi:10.1002/hyp.1067.

Wiscombe, W. J., and S. G. Warren (1980), A model for the spectral albedo of snow. part I: Pure snow, *J. Atmos. Sci.*, 37, 2712–2733, doi:10.1175/1520-0469(1980)037<2712:AMFTSA>2.0.CO;2.

————————————

F. S. Anslow, Department of Earth and Ocean Sciences, University of British Columbia, 6339 Stores Road, Vancouver, BC, Canada V6T 1Z4. (fanslow@eos.ubc.ca)

W. R. Bidlake, United States Geological Survey, Washington Water Science Center, 934 Broadway, Suite 300, Tacoma, WA 98402, USA.

P. U. Clark, Department of Geosciences, Oregon State University, 104 Wilkinson Hall, Corvallis, OR 97331, USA.

S. Hostetler, United States Geological Survey, Department of Geosciences, Oregon State University, 104 Wilkinson Hall, Corvallis, OR 97331, USA.